



2021

**The  $\text{Na}_x\text{MnO}_2$  materials prepared by a glycine-nitrate method as advanced cathode materials for aqueous sodium-ion rechargeable batteries**

Rakočević, L., Štrbac, S., Potočnik, J., Popović, M., Jugović, D., & Stojković Simatović, I.

*Published in:*

Ceramics International

*DOI:*

[10.1016/j.ceramint.2020.10.025](https://doi.org/10.1016/j.ceramint.2020.10.025)

*Document version:*

Peer reviewed article (often known as postprint article)

*Recommended citation:*

Rakočević, L., Štrbac, S., Potočnik, J., Popović, M., Jugović, D., & Simatović, I. S. (2021). The  $\text{Na}_x\text{MnO}_2$  materials prepared by a glycine-nitrate method as advanced cathode materials for aqueous sodium-ion rechargeable batteries. *Ceramics International*, 47(4), 4595-4603.

This work is licenced under [Creative Commons Attribution-Noncommercial-NoDerivates 4.0 International Licence](https://creativecommons.org/licenses/by-nc-nd/4.0/)



1  
2  
3  
4 **The Na<sub>x</sub>MnO<sub>2</sub> Materials Prepared by a Glycine-nitrate Method as**  
5  
6  
7 **Advanced Cathode Materials for Aqueous Sodium-Ion Rechargeable**  
8  
9  
10 **Batteries**

11  
12 Lazar Rakočević<sup>a</sup>, Svetlana Štrbac<sup>b</sup>, Jelena Potočnik<sup>a</sup>, Maja Popović<sup>a</sup>, Dragana Jugović<sup>c</sup>,  
13  
14 Ivana Stojković Simatović<sup>d,\*</sup>  
15

16  
17 <sup>a</sup>INN Vinca, Laboratory of Atomic Physics, University of Belgrade, Mike Alasa 12-14, 11001 Belgrade, Serbia

18  
19 <sup>b</sup>IHTM-Institute of Electrochemistry, University of Belgrade, Njegoševa 12, 11000 Belgrade, Serbia

20  
21 <sup>c</sup>Institute of Technical Sciences of SASA, Belgrade, Serbia

22  
23 <sup>d</sup>Faculty of Physical Chemistry, University of Belgrade, Studentski trg 12-16, 11158 Belgrade, Serbia  
24  
25  
26  
27

28 **Abstract**

29  
30 Cathodic materials for sodium-ion rechargeable batteries based on Na<sub>x</sub>MnO<sub>2</sub> were  
31 synthesized by glycine nitrate method and subsequent annealing at high temperatures. Different  
32 crystal structures with different morphologies were obtained depending on the annealing  
33 temperature: hexagonal layered  $\alpha$ -Na<sub>0.7</sub>MnO<sub>2.05</sub> nanoplates were obtained at 850 °C, while 3-D  
34 tunnel structured Na<sub>0.4</sub>MnO<sub>2</sub> and Na<sub>0.44</sub>MnO<sub>2</sub>, both with rod-like morphology, were obtained at  
35 800 °C and 900 °C, respectively. The investigations of the electrochemical behavior of obtained  
36 cathodic materials in aqueous NaNO<sub>3</sub> solution have shown that Na<sub>0.44</sub>MnO<sub>2</sub> obtained at 900 °C  
37 has shown the best battery performance. Its initial discharge capacities are 123.5 mAh/g, 113.2  
38 mAh/g, and 102.0 mAh/g at the high current densities of 1000, 2000 and 5000 mA/g,  
39 respectively.  
40  
41  
42  
43  
44  
45  
46  
47  
48  
49  
50  
51  
52  
53

54  
55 *Keywords:* aqueous sodium-ion batteries; cathode material; sodium manganese oxide;  
56  
57 nanoplates; nanorods.  
58

59  
60 *\*Corresponding author: E-mail: [ivana@ffh.bg.ac.rs](mailto:ivana@ffh.bg.ac.rs)*  
61  
62  
63  
64  
65

## 1. Introduction

Increasing energy consumption, as well as an increasing concern for the environment, requires the development of renewable energy sources. Among electrochemical energy storage systems, rechargeable batteries, particularly lithium-ion batteries are the most commonly used as the energy source in portable devices and electric vehicles [1,2]. Since lithium is relatively rare on earth but rapidly consumed, it is necessary to find an adequate replacement. Owing to the similar chemical properties of sodium and lithium, but much higher availability, sodium-ion batteries are one of the best candidates to replace lithium-ion batteries [3]. Both types of batteries contain a unique pair of cathode composed of Li or Na ion intercalation material, and an anode composed of carbon material, the performance of which is studied in a half cell [4-6]. In sodium-ion batteries, transition metal (M=Mn, Co, Fe, Ni) oxides or polyanionic compounds containing metal (Fe, Co, Mn, V) and phosphates or sulfates are used as a cathode [4,6], while hard carbon is the most commonly used anode material [5]. Among transition metal oxides, the best candidates as cathodic materials are those with either tunnel or layered structure, which enable a reversible  $\text{Na}^+$ -ion intercalation/deintercalation without a significant structural change [4,6]. Moreover, it is also necessary to replace traditionally used highly toxic and flammable organic solvents with aqueous electrolytes, which gives rise to a rapid progress of aqueous Li-ion batteries, and most recently of aqueous Na-ion batteries [7-10].

As a potential cathode material in Na-ion rechargeable batteries, different sodium manganese oxides (Na-Mn-O) have recently attracted a lot of attention [11-13]. Depending on sodium to manganese ratio and temperature, a variety of Na-Mn-O compounds can be synthesized, which was reported for the first time in ref. [14]. Namely, several new ternary

1  
2  
3  
4 oxides of  $\text{Na}_x\text{MnO}_2$  type were synthesized, in which the ratio of sodium to manganese  $\text{Na}/\text{Mn} \leq$   
5  
6  
7 1:  $\text{Na}_{0.20}\text{MnO}_2$ ,  $\text{Na}_{0.40}\text{MnO}_2$ ,  $\text{Na}_{0.44}\text{MnO}_2$ ,  $\text{Na}_{0.70}\text{MnO}_{2+y}$ , ( $0 \leq y \leq 0.25$ ) and  $\text{NaMnO}_2$ , the latter  
8  
9 two with two allotropes of  $\alpha$  and  $\beta$ . In the same paper [14], the phase diagram was given  
10  
11 resulting from the stability of these compounds concerning the  $\text{Na}/\text{Mn}$  ratio and temperature.  
12

13  
14  $\text{Na}_x\text{MnO}_2$  compounds with different crystal structure and morphology can be prepared by  
15  
16 various methods. For example, hexagonal-layered  $\text{Na}_{0.7}\text{MnO}_{2.05}$  can be prepared by solvothermal  
17  
18 synthesis [15]. Tunnel structured  $\text{Na}_{0.44}\text{MnO}_2$  with rod-like morphology can be prepared by solid-  
19  
20 state synthesis at high temperatures [16], while one-dimensional single-crystalline  $\text{Na}_{0.44}\text{MnO}_2$   
21  
22 nanowires were produced by low-temperature hydrothermal synthesis [17]. Well-defined single-  
23  
24 crystalline  $\text{Na}_{0.44}\text{MnO}_2$  nanowires and nanorods were obtained by polymer pyrolysis method and  
25  
26 subsequent annealing at higher temperatures [18], while  $\text{Na}_{0.44}\text{MnO}_2$  nanoribbons can be prepared  
27  
28 by  $\text{NaCl}$ -flux reaction at  $850^\circ\text{C}$  [19]. Tunnel structured  $\text{Na}_{0.4}\text{MnO}_2$  with well-defined rod-like  
29  
30 morphology can be prepared by a conventional solid-state synthesis [14], glycine-nitrate method  
31  
32 [20], or through alkaline hydrolysis [21], in all cases followed by annealing at temperatures  
33  
34 below  $750^\circ\text{C}$ .  
35  
36  
37  
38  
39  
40

41 The main electrochemical properties of  $\text{Na-Mn-O}$  cathode materials involve their cycling  
42  
43 performance and reversible capacity. The performance of these compounds as the cathode  
44  
45 material in  $\text{Na-ion}$  batteries in both non-aqueous and aqueous electrolytes mainly depends on  
46  
47 their crystal structure and morphology. The following research reports relate to the behavior of  
48  
49  $\text{Na-Mn-O}$  cathode materials in non-aqueous electrolytes (1 M  $\text{NaClO}_4$  dissolved in a mixture of  
50  
51 organic solvents). For instance, layered  $\text{Na}_{0.7}\text{MnO}_2$  nanoplates exhibit a high reversible capacity  
52  
53 of 163  $\text{mAh/g}$ , and a satisfactory cyclability [22]. Single crystalline tunnel structured  $\text{Na}_{0.44}\text{MnO}_2$   
54  
55 nanowires and nanorods obtained after annealing at  $750^\circ\text{C}$  have shown exceptional cyclic  
56  
57  
58  
59  
60  
61  
62  
63  
64  
65



1  
2  
3  
4 performance (77% capacity retention for 1000 cycles for charge/discharge current density of 60  
5 mA/g), and high reversible capacity of 128 mAh/g for 12 mA/g [18]. Na<sub>0.44</sub>MnO<sub>2</sub> nanoribbons  
6  
7 have shown a high capacity of 106 mAh/g, with stable cycling performance [19]. Tunnel  
8  
9 structured Na<sub>0.4</sub>MnO<sub>2</sub> nanorods show good cycle performance, and an initial discharge capacity  
10  
11 of 83.7 mAh/g at 12mA/g, and maintains 84.7% after 50 cycles [23]. On the other hand,  
12  
13 Na<sub>0.44</sub>MnO<sub>2</sub> nanorods synthesized using modified Pechini method shows better rate capability in  
14  
15 aqueous (0.5 M Na<sub>2</sub>SO<sub>4</sub>) than in non-aqueous electrolyte [24]. Research on the behavior of Na-  
16  
17 Mn-O cathode materials in aqueous electrolytes has gained momentum only recently, and a brief  
18  
19 overview of the latest research will be given. Tunnel structured Na<sub>0.4</sub>MnO<sub>2</sub> rods have shown the  
20  
21 initial discharge capacity of 38 mAh/g, with good cycling performance in aqueous 1 M NaClO<sub>4</sub>  
22  
23 solutions [25]. Hexagonal layered Na<sub>0.7</sub>MnO<sub>2</sub> nanoplates have shown an initial specific discharge  
24  
25 capacity of 125 mAh/g in 1 M Na<sub>2</sub>SO<sub>4</sub> solution during charge/discharge cycling [15]. Finally, the  
26  
27 most intensively studied Na<sub>0.44</sub>MnO<sub>2</sub> nanorods have shown the capacity of 80 mAh/g in 3 M  
28  
29 ZnSO<sub>4</sub> solution [26]. In an aqueous NaNO<sub>3</sub> solution (pH = 13.5), the initial capacity was 40  
30  
31 mAh/g [27]. Besides, as the cathode in alkaline Zn-Na<sub>0.44</sub>MnO<sub>2</sub> dual-ion battery, it has shown  
32  
33 excellent electrochemical performance with high reversible capacity of 80.2 mAh/g and  
34  
35 outstanding cycling stability in 6 M NaOH aqueous electrolyte [28].  
36  
37  
38  
39  
40  
41  
42  
43  
44

45 In this work, different Na<sub>x</sub>MnO<sub>2</sub> powders will be synthesized by glycine-nitrate method  
46  
47 (GNM). Such precursor powders will be annealed at three different temperatures: 800 °C, 850  
48  
49 °C, and 900 °C. Na<sub>x</sub>MnO<sub>2</sub> compounds with different crystal structures will be obtained,  
50  
51 depending on the annealing temperature. X-ray diffraction technique (XRD) will be used for the  
52  
53 determination of crystal structure of synthesized powders while scanning electron microscopy  
54  
55 with energy-dispersive X-ray spectroscopy (SEM/EDS) will be employed for powders  
56  
57  
58  
59  
60  
61  
62  
63  
64  
65

1  
2  
3  
4 morphology and elemental analyses. Additionally, chemical analysis including the oxidation  
5 state of the obtained compounds constituents will be determined by X-ray photoemission  
6 spectroscopy. Electrochemical properties will be tested by cyclic voltammetry and  
7 chronopotentiometry in an aqueous NaNO<sub>3</sub> solution. Materials obtained by annealing at different  
8 temperatures will be compared with each other with a special emphasis on the effect of the  
9 structure and morphology on their electrochemical performance (cycling reversibility, efficiency,  
10 charge/discharge speed, and specific capacity) for potential use in sodium-ion aqueous batteries.  
11  
12  
13  
14  
15  
16  
17  
18  
19  
20  
21  
22

## 23 **2. Experimental**

### 24 *2.1. Synthesis of Na<sub>x</sub>MnO<sub>2</sub> powders*

25  
26  
27  
28  
29  
30  
31  
32  
33 The synthesis of Na<sub>x</sub>MnO<sub>2</sub> powders was performed by the glycine-nitrate method.  
34 Aqueous solutions of 2.45 ml 1 M NaNO<sub>3</sub> (Merck) and 5.10 ml 0.96 M Mn(NO<sub>3</sub>)<sub>2</sub> (Merck) were  
35 mixed, and then the solid glycine (Merck) was added to the mixture in the molar ratio of 1.2: 1 to  
36 nitrate (1.104 g of glycine). The resulting solution was then heated in an oven at 200 °C until the  
37 spontaneous combustion. The obtained ash was annealed for four hours at different temperatures:  
38 800 °C, 850 °C, or 900 °C. Thus prepared Na<sub>x</sub>MnO<sub>2</sub> powders were further used either for *ex-situ*  
39 characterization or the preparation of a working electrode for electrochemical measurements.  
40  
41  
42  
43  
44  
45  
46  
47  
48  
49  
50  
51  
52

### 53 *2.2. Structural, morphological and chemical characterization of Na<sub>x</sub>MnO<sub>2</sub> powders*

#### 54 *2.2.1. XRD characterization*

1  
2  
3  
4 Crystal structure and qualitative phase identification of as prepared  $\text{Na}_x\text{MnO}_2$  powders  
5  
6 were analyzed by X-ray diffraction technique using Philips PW-1050 diffractometer with CuK $\alpha$   
7  
8 emission width  $\lambda = 0.15418$  nm. For all powder samples, data were collected in the  $2\theta$  range of  
9  
10  $10^\circ - 70^\circ$  with the step of  $0.05^\circ$  and the dwell time of 5s. The analysis of obtained powder patterns  
11  
12 was performed by comparison to known powder patterns.  
13  
14  
15  
16  
17  
18

### 19 *2.2.2. SEM/EDS characterization*

20

21 Particle morphology and the particle size distribution of as prepared  $\text{Na}_x\text{MnO}_2$  powders  
22  
23 were analyzed using Field emission scanning electron microscopy (FESEM) technique, while  
24  
25 chemical composition including surface chemical mapping was analyzed by Energy dispersive  
26  
27 spectrometry (EDS) technique, both using FEI SCIOS 2 Dual Beam microscope. The powder  
28  
29 was pressed into a copper double-sided adhesive tape to provide mechanical support and  
30  
31 electrical contact and then recorded under high vacuum with an accelerating voltage of 10 kV.  
32  
33  
34  
35  
36  
37

### 38 *2.2.3. XPS measurements*

39

40  
41 As received  $\text{Na}_x\text{MnO}_2$  powders were analyzed without any treatment. The powder was  
42  
43 pressed onto a copper double-sided adhesive tape to provide mechanical support and electrical  
44  
45 contact. Binding energies were corrected using for calibration the position of C1s peak located at  
46  
47 284.8 eV (for adventitious carbon originating from impurities due to exposure to air).  
48  
49

50  
51 XPS measurements were carried out using the SPECS system with a monochromatic  
52  
53 source of X-radiation (AlK $\alpha$  line with photon energy of 1486.3 eV). Survey spectra were  
54  
55 recorded in FAT40 mode with step energy of 0.5 eV, and the acquisition time of 0.2  
56  
57 s/channel. High-resolution spectra of the main photoelectron lines for Na, Mn, and O are  
58  
59  
60  
61  
62  
63  
64  
65

1  
2  
3  
4 recorded in the FAT20 mode with the step energy of 0.1 eV, and the acquisition time of 2  
5  
6 s/channel. The pressure in the analysis chamber was kept at  $10^{-8}$  mbar during the measurements.  
7  
8  
9

### 10 11 *2.3. Electrochemical measurements*

#### 12 13 14 *2.3.1. Working electrode preparation*

15  
16 The suspension for the working electrode was prepared by mixing 85% of the powder  
17  
18 sample, 10% of the carbon black (VulcanXC72, Cabot Corp.), and 5% polyvinylidene fluoride  
19  
20 (PVDF) in a 2% solution of N-methyl-2-pyrrolidone (Merck). After homogenization in an  
21  
22 ultrasonic bath, the suspension was smeared as a thin layer over a glassy carbon electrode  
23  
24 (geometric area=  $1.2 \text{ cm}^2$ ) and dried under vacuum for 4 h at the temperature of  $140 \text{ }^\circ\text{C}$ . The  
25  
26 resulting amount of the material synthesized at 800, 850 or  $900 \text{ }^\circ\text{C}$  obtained by subtracting the  
27  
28 weight of the bare glassy carbon substrate, were 1.11, 1.23 and 1.36 mg, respectively.  
29  
30  
31  
32  
33

#### 34 35 36 *2.3.2. Cyclic voltammetry measurements*

37  
38 Electrochemical characterization was performed using Gamry PCI4/750 in a three-  
39  
40 electrode cell consisting of a working electrode, platinum foil as a counter electrode and a  
41  
42 saturated calomel electrode (SCE) as a reference electrode. Cyclic voltammograms were  
43  
44 recorded in an aqueous 6 M  $\text{NaNO}_3$  electrolyte in the potential range from -1.30 V to 1.35 V, and  
45  
46 using different sweep rates in the range from 20 mV/s to 400 mV/s.  
47  
48  
49  
50

#### 51 52 53 *2.3.3. Chronopotentiometry measurements*

54  
55 Chronopotentiometry technique was used for the evaluation of charge/discharge behavior  
56  
57 of obtained  $\text{Na}_x\text{MnO}_2$  electrodes. Measurements were performed using Gamry PCI4/750  
58  
59  
60  
61  
62  
63  
64  
65

1  
2  
3  
4 potentiostat in saturated aqueous NaNO<sub>3</sub> solution. Five cycles were recorded for each electrode in  
5  
6 the potential range from -1.00 V to 1.25 V, and applying the current densities of 1000, 2000 and  
7  
8 5000 mA/g.  
9

### 10 11 12 13 14 **3. Results and discussion** 15

#### 16 17 18 19 *3.1. Crystal structure and morphology of Na<sub>x</sub>MnO<sub>2</sub> powders* 20

21 XRD diffractograms of Na<sub>x</sub>MnO<sub>2</sub> powder samples synthesized at 800 °C, 850 °C, and  
22  
23 900 °C are shown in Fig. 1, where each crystallographic plane is labeled by Miller indexes (hkl).  
24  
25 Sharp peaks in all XRD patterns indicate that the obtained powders consist of highly crystalline  
26  
27 phases, the structure of which differ and depend on the annealing temperature. SEM  
28  
29 microphotographs showing the morphology of each obtained Na<sub>x</sub>MnO<sub>2</sub> powder samples are also  
30  
31 shown in Fig.1.  
32  
33

34  
35 According to the positions of the reflections in the diffractogram, and when compared to  
36  
37 the known reference diffractograms, the powder sample synthesized at 800 °C, Fig. 1a, is  
38  
39 identified as orthorhombic Na<sub>0.4</sub>MnO<sub>2</sub> [JCPDS 27-0749] with a tunnel structure of a  
40  
41 romanechite type [14,21]. It was reported earlier that such a structure consists of (3 x 2) tunnels  
42  
43 with MnO<sub>6</sub> octahedral units shared by corners and/or edges [14,20,21,23]. Apart from the  
44  
45 reflections corresponding to the Na<sub>0.4</sub>MnO<sub>2</sub> compound (marked in red), the ones indicating the  
46  
47 presence of impurities as a side product during synthesis are also identified. Among impurities,  
48  
49 peaks corresponding to Mn<sub>2</sub>O<sub>3</sub> [JCPD 31-0825] [29,30] are observed (marked in blue) as  
50  
51 expected from a phase diagram [14], as well as peaks at 37° and 65.6° (marked in black) which  
52  
53 are assigned to (121) and (002) crystallographic planes corresponding to α-MnO<sub>2</sub> phase (JCPDS-  
54  
55  
56  
57  
58  
59  
60  
61  
62  
63  
64  
65

1  
2  
3  
4 72-1982) [31]. SEM micrograph showing the morphology of  $\text{Na}_{0.4}\text{MnO}_2$  powder synthesized at  
5  
6  
7 800 °C is given in Fig. 1b. Uniformly shaped rod-like structures with the size on a nanometer  
8  
9 scale are observed. Such nanorods are 200 to 700 nm long and 60 to 110 nm wide.

10  
11 The diffraction pattern for powder obtained at 850 °C, Fig. 1c, corresponds to the  
12 reference diffractogram [JCPDS 27-0751] of pure highly crystalline hexagonal-layered  $\alpha$ -  
13  
14  $\text{Na}_{0.7}\text{MnO}_{2.05}$  [15,32]. This layered structure is composed of edge-sharing  $\text{MnO}_6$  octahedra  
15  
16 forming  $(\text{MnO}_2)_n$  sheets and sodium ions situated between these sheets [15]. Additional  
17  
18 reflections, that can also be observed, are ascribed to  $\text{MnO}_2$  phase which is indexed to the  
19  
20 tetragonal system [JCPDS 72-1982]. SEM microphotographs of  $\text{Na}_{0.7}\text{MnO}_{2.05}$  powder  
21  
22 synthesized at 850 °C are given in Fig. 1d. It can be seen that the resulting crystalline particles  
23  
24 have mostly regular hexagonal-platelet morphology with the size on a nanometer scale. Such  
25  
26 hexagonal nanoplates are rather uniform in size with a radius ranging from 500 nm up to 1.5  $\mu\text{m}$   
27  
28 and a thickness ranging from 200 nm up to 500 nm.

29  
30  
31 Powder obtained at 900 °C, Fig. 1e, is identified as pure highly crystalline orthorhombic  
32  
33  $\text{Na}_{0.44}\text{MnO}_2$  [JCPDS 27-0750], which is in agreement with diffractograms of the same compound  
34  
35 reported earlier [16,24,33]. Crystal structure of  $\text{Na}_{0.44}\text{MnO}_2$  is already well described [16,19,24,  
36  
37 27,33], and briefly, it consists of double and triple chains of a rutile type with octahedral  $\text{MnO}_6$   
38  
39 molecules on edges and single chains,  $\text{MnO}_5$  polyhedrons on edges, and Na situated in tunnels.  
40  
41 Its unique tunnel structure is suitable for  $\text{Na}^+$  ions intercalation/deintercalation [16,18,24]. SEM  
42  
43 micrographs of  $\text{Na}_{0.44}\text{MnO}_2$  powder obtained at 900 °C is given in Fig. 1f. It can be seen that they  
44  
45 are rod-like shaped, with rods approximately a few  $\mu\text{m}$  long and few hundred nm wide.  
46  
47  
48  
49  
50  
51  
52  
53  
54  
55  
56  
57

### 58 3.2. Chemical analysis of $\text{Na}_x\text{MnO}_2$ powders

59  
60  
61  
62  
63  
64  
65

1  
2  
3  
4 *3.2.1. EDS spectra and the elemental mapping*  
5  
6

7           Chemical analysis of the samples obtained by the mapping technique is shown in Fig. 2.  
8  
9           The spatial distribution of the various elements present in the  $\text{Na}_x\text{MnO}_2$  powders was determined  
10 by the elemental mapping. Different colors were used to visually distinguish the presence of  
11 sodium (purple), manganese (red) and oxygen (green). Mapping shows that Na, Mn and O are  
12 located exactly on those parts of the surface which correspond to the structure seen in the SEM  
13 micrographs, which confirms that they consist of these elements. Unlike sodium and oxygen,  
14 manganese partly arises out of the surface of the structures visible in SEM micrographs, which  
15 originates from Mn at a greater depth due to the higher ability of Mn to reflect electrons as  
16 compared to Na and O.  
17  
18  
19  
20  
21  
22  
23  
24  
25  
26  
27  
28  
29  
30

31 *3.2.2. XPS measurements*  
32

33           The survey spectrum of  $\text{Na}_x\text{MnO}_2$  powders synthesized at different temperatures is given  
34 in Fig. 3. The spectrum clearly shows the basic photoelectron and Auger lines of sodium (Na 1s,  
35 Na CLL), manganese (Mn2p, Mn LMM), and oxygen (O1s, O-CLL). Besides, the C1s line of  
36 carbon, as typical contamination present in each sample is also recorded. It should be noted that  
37 the Na Auger lines are located close to the main oxygen line.  
38  
39  
40  
41  
42  
43  
44

45           High-resolution spectra of Mn2p, Na1s and O1s lines as constitutive elements of each  
46 synthesized  $\text{Na}_x\text{MnO}_2$  powder are given in Fig. 4. To precisely identify the oxidation states of  
47 these elements, the spectra are deconvoluted and analyzed. Due to the effect of the spin-orbit  
48 coupling Mn2p lines doubled and consists of two components: Mn2p<sub>3/2</sub> and Mn2p<sub>1/2</sub>. The line  
49 Mn2p<sub>3/2</sub> is fitted using GL(30) pseudo-Voigt profile (30% Lorentzian, 70% Gaussian) with a  
50 Shirley background.  
51  
52  
53  
54  
55  
56  
57  
58  
59  
60  
61  
62  
63  
64  
65

1  
2  
3  
4 For  $\text{Na}_{0.4}\text{MnO}_2$  synthesized at 800 °C, Fig. 4a,  $\text{Mn}2p_{3/2}$  photoelectron line is fitted to three  
5 contributions: 641.2 eV, 642.4, and 643.8 eV. In the insets of Fig. 4a, Na1s, and O1s  
6 photoelectron lines are presented. Na1s line is fitted to two contributions: 1070.9 eV (marked by  
7 1) and 1072.4 eV (marked by 2), while O1s line is fitted to four contributions: 529.7 eV (marked  
8 by 1), 531.3 eV (marked by 2), 532.5 eV (marked by 3) and 533.5 eV (marked by 4). The first  
9 Na1s line at lower binding energies corresponds to metal Na, while the second one at higher  
10 binding energies corresponds to NaOH following the third O1s peak at 532.5 eV originating  
11 from H-O-Na bonding [34,35]. According to literature data [36,37], the first  $\text{Mn}2p_{3/2}$  peak at  
12 641.2 eV corresponds to either  $\text{MnOOH}$  (manganite, 641.2 eV in ref. [36], and 641.4 in ref.[37] )  
13 or to  $\text{Mn}_2\text{O}_3$  (640.8 eV in ref. [36], and 641.2 eV in ref. [38]). Since no  $\text{MnOOH}$ , but rather  
14  $\text{Mn}_2\text{O}_3$  is positively identified by XRD (see Fig.1), this peak can be ascribed to manganese (III),  
15 which is also consistent with the fact that the decomposition of  $\text{MnOOH}$  into  $\text{Mn}_2\text{O}_3$  occurs  
16 already at 250°C [38]. Besides, this peak is most likely superimposed to the Mn(III) component  
17 in pyrolusite (tunnel structured manganese mineral hollandite) [36], and both peaks correspond  
18 to the first O1s peak at 529.7 eV. The second and third peaks at 642.4 eV and 643.7 eV,  
19 respectively correspond to two components of manganese (IV) multiplet structure as shown in  
20 ref. [32]. The one at lower binding energy (also in agreement with 642.5 eV in refs. [36, 38], and  
21 642.2 eV in ref. [39] can be ascribed to  $\text{MnO}_2$  following also the first O1s peak [40]. The one at  
22 higher binding energies (peaks at 643.5 eV and 644.3 eV in ref. [36]) can be ascribed to Mn(IV)  
23 originating from pyrolusite following the second O1s peak at 531.3 eV for oxygen originating  
24 from Na-Mn-O bonding [39]. It should be noted that the fourth O1s line can be ascribed to  
25 oxygen from adsorbed water [41], and appears in all investigated  $\text{Na}_x\text{MnO}_2$  compounds.  
26  
27  
28  
29  
30  
31  
32  
33  
34  
35  
36  
37  
38  
39  
40  
41  
42  
43  
44  
45  
46  
47  
48  
49  
50  
51  
52  
53  
54  
55  
56  
57  
58  
59  
60  
61  
62  
63  
64  
65



1  
2  
3  
4 For  $\text{Na}_{0.7}\text{MnO}_{2.05}$  synthesized at 850 °C, Fig. 4b,  $\text{Mn}2p_{3/2}$  photoelectron line is fitted to  
5 two contributions: 642.6 eV, and 644.1 eV. In the insets of Fig. 4b, Na 1s photoelectron line is  
6 fitted to two contributions: 1071.9 eV and 1073.9 eV, while O1s line is fitted to four  
7 contributions: 530.1 eV (1), 531.7 eV (2), 532.8 eV (3) and 534.1 eV (4).  $\text{Mn}2p_{3/2}$  photoelectron  
8 lines can be ascribed to two Mn(IV) contributions in birnessite (layer structured manganese  
9 mineral) [36], and correspond with the first and second O1s lines, respectively. Like in the  
10 previous case, the first Na1s lines ascribed to metal Na and the second to NaOH following the  
11 third O1s peak[34].  
12  
13  
14  
15  
16  
17  
18  
19  
20  
21  
22

23  
24 For  $\text{Na}_{0.44}\text{MnO}_2$  synthesized at 900 °C, Fig. 4c,  $\text{Mn}2p_{3/2}$  line is fitted to three  
25 contributions: 641.2 eV, 642.4, and 643.7 eV, which are equal or very close to the values  
26 obtained for  $\text{Na}_{0.4}\text{MnO}_2$  synthesized at 800 °C, meaning that the peaks correspond to Mn(III) and  
27 two Mn(IV) contributions, respectively. In the insets of Fig. 4c, Na 1s photoelectron line is fitted  
28 to only one contribution at 1071.9 eV corresponding to metal Na meaning that no traces of  
29 NaOH are observed after the annealing at 900°C. O1s line is fitted to three contributions: 530.0  
30 eV (1), 531.5 eV (2), and 534.0 eV (4), which are in agreement with binding energies as in the  
31 case of  $\text{Na}_{0.4}\text{MnO}_2$ , and can be interpreted in the same way.  
32  
33  
34  
35  
36  
37  
38  
39  
40  
41  
42  
43  
44

### 45 *3.3. Electrochemical behavior of $\text{Na}_x\text{MnO}_2$ in aqueous electrolyte*

#### 46 *3.3.1. Cyclic voltammetry of $\text{Na}_x\text{MnO}_2$ electrodes*

47  
48 The electrochemical behavior of all prepared  $\text{Na}_x\text{MnO}_2$  electrodes was investigated by  
49 cyclic voltammetry in a saturated aqueous  $\text{NaNO}_3$  solution. Cyclic voltammograms (CVs) were  
50 recorded during continuous cycling of the potential with a sweep rate of 20 mV/s. CVs for  
51  $\text{Na}_x\text{MnO}_2$  synthesized at 800 °C, 850 °C, and 900 °C are given in Fig. 5.  
52  
53  
54  
55  
56  
57  
58  
59  
60  
61  
62  
63  
64  
65

1  
2  
3  
4 In all CVs, cathodic peaks corresponding to the process of Na<sup>+</sup>-ions intercalation, as well  
5  
6 as anodic peaks corresponding to the process of Na<sup>+</sup>-ions deintercalation can be observed. The  
7  
8 electrochemical reaction of Na<sup>+</sup> intercalation/deintercalation on the cathode can be expressed as  
9  
10  
11 [4]:



13  
14  
15 where: x is the number of inserted Na<sup>+</sup> ions. Cathodic peaks correspond to the formation of Na<sub>x-</sub>  
16  
17  
18  
19  
20  
21  
22  
23  
24  
25  
26  
27  
28  
29  
30  
31  
32  
33  
34  
35  
36  
37  
38  
39  
40  
41  
42  
43  
44  
45  
46  
47  
48  
49  
50  
51  
52  
53  
54  
55  
56  
57  
58  
59  
60  
61  
62  
63  
64  
65

21 The number, shape, position, and intensity of various cathodic/anodic peaks indicate that  
22  
23  
24 there are various processes of Na<sup>+</sup>-ions intercalation/deintercalation, which take place in many  
25  
26  
27 electrochemical steps. The shape of CVs for all different Na<sub>x</sub>MnO<sub>2</sub> electrodes synthesized at  
28  
29  
30 different temperatures is changing during cycling.

31 For each Na<sub>x</sub>MnO<sub>2</sub> electrode, independent of the synthesis temperature, cyclic  
32  
33  
34  
35  
36  
37  
38  
39  
40  
41  
42  
43  
44  
45  
46  
47  
48  
49  
50  
51  
52  
53  
54  
55  
56  
57  
58  
59  
60  
61  
62  
63  
64  
65

48 For Na<sub>0.4</sub>MnO<sub>2</sub> synthesized at 800 °C, Fig. 5a, the cathodic and anodic positions of peaks  
49  
50  
51  
52  
53  
54  
55  
56  
57  
58  
59  
60  
61  
62  
63  
64  
65

ions intercalation/deintercalation. Besides, the intensity of each peak increases with continuing cycling.

The shape of CV for  $\text{Na}_{0.7}\text{MnO}_{2.05}$  synthesized at  $850\text{ }^{\circ}\text{C}$ , Fig. 5b, is changing rapidly after the first cycle showing much higher current densities in the whole potential region. A significant change is observed in the peak I, where its cathodic part at  $-0.7\text{ V}$ , which is particularly pronounced in the first cycle, decreases and finally disappears up to the tenth cycle. At the same time, a new cathodic peak arises at approx.  $-0.4\text{ V}$ , and increases up to the tenth cycle. Besides, the first anodic peak at approx.  $0.01\text{ V}$  increases significantly after the first cycle, but then decreases with further cycling. These changes which were described as the initial electrode activation similarly like in the case of  $\text{Na}_{0.6}\text{MnO}_2$  [42], can be attributed to the phase transition from  $\text{Na}_{0.7}\text{MnO}_{2.05}$  to  $\text{Na}_{0.9}\text{MnO}_{2.05}$  [15]. After the tenth cycle, the shape of CVs stabilizes, and positions of cathodic and anodic parts of peaks I and III ( $0.37\text{ V}/-0.01\text{ V}$ , and ( $-0.98\text{ V}/1.3\text{ V}$ ), as well as their intensity change negligible.

In CVs of  $\text{Na}_{0.44}\text{MnO}_2$  synthesized at  $900\text{ }^{\circ}\text{C}$ , Fig. 5c, starting from the first up to the tenth cycle, the positions of cathodic and anodic parts of peaks I ( $-0.3\text{ V}/0.07\text{ V}$ ) and III ( $0.97\text{ V}/1.1\text{ V}$ ), are only slightly changed during cycling. Since these peaks correspond to the  $\text{Na}^+$  ions intercalation/deintercalation processes there is a good cycling reversibility. On the other hand, the intensities of both cathodic and anodic peaks increase significantly during cycling indicating the improvement in charge/discharge capacity, most likely due to the phase transition to  $\text{Na}_{0.33}\text{MnO}_2$ , which occurs in  $0.01\text{ M NaNO}_3$  aqueous electrolyte as reported in ref. [43].

Cyclic voltammograms of the same  $\text{Na}_x\text{MnO}_2$  electrodes, recorded under the same conditions but with different sweep rates ranging from  $20$  to  $400\text{ mV/s}$ , are given in Fig. 6 (a,d,g). For comparison, the current density scales, as well as potential scales are the same in all

1  
2  
3  
4 cases. For each  $\text{Na}_x\text{MnO}_2$  electrodes, the shapes of CVs concerning peak positions are similar for  
5  
6 all sweep rates. Current densities are similar for  $\text{Na}_{0.4}\text{MnO}_2$  synthesized at  $800\text{ }^\circ\text{C}$ , Fig. 6a, and  
7  
8  $\text{Na}_{0.7}\text{MnO}_{2.05}$  synthesized at  $850\text{ }^\circ\text{C}$ , Fig. 6d, and increase in a similar extent with increasing  
9  
10 sweep rate. On the other hand, current densities for  $\text{Na}_{0.44}\text{MnO}_2$  synthesized at  $900\text{ }^\circ\text{C}$ , Fig. 6g,  
11  
12 increase much more with increasing sweep rate, meaning that the reversibility of  $\text{Na}^+$  ions  
13  
14 intercalation/deintercalation is maintained even for higher charge/discharge rates.  
15  
16  
17  
18

19 CV curves at different current rates were used to analyze the electrochemical kinetics of  
20  
21 synthesized materials. The area of a CV curve slowly increased, with the reduction and oxidation  
22  
23 peaks shifted to lower and higher voltages, respectively. The ratio of capacitive and faradaic  
24  
25 processes can be determined based on the value of the constant  $b$  obtained from equation [25,  
26  
27 26, 44]  $i = av^b$  where  $a$  and  $b$  are adjustable values. The value of  $b \sim 0.5$  is characteristic for the  
28  
29 full diffusion-controlled process, while  $b \sim 1$  is characteristic for the full capacitive controlled  
30  
31 process. The constant  $b$  was calculated as the slope of the  $\log(i)$  vs.  $\log(v)$  plots, Fig 6 (b,e,h).  
32  
33 For all samples, the value of  $b$  indicates that the corresponding redox reactions during the charge  
34  
35 and discharge processes were combined capacitive and intercalation reactions [25]. For  
36  
37  $\text{Na}_{0.44}\text{MnO}_2$ ,  $b$  was the smallest and its values for discharge and charge process were 0.63 and  
38  
39 0.71, respectively, which suggested more favored diffusion kinetics of  $\text{Na}_{0.44}\text{MnO}_2$ . The  
40  
41 percentage of capacitive and diffusion contribution is determined by the following equation  
42  
43 [26, 44]  $i(v) = k_1v + k_2v^{1/2}$  where  $k_1$  and  $k_2$  are constants. The  $k_1v$  and  $k_2v^{1/2}$  represent the  
44  
45 capacitive and the diffusion controlled contribution, respectively. For all samples, with the  
46  
47 increase of the scan rate, the diffusion contribution decreased, while the capacitive contribution  
48  
49 increased, Fig. 6 (c,f,i). Accordingly, the capacitive contribution of  $\text{Na}_{0.44}\text{MnO}_2$  at scan rate of  
50  
51 50 mV/s was 48.1% and up to 72.5% at 400 mV/s, Fig. 6 (i). A similar ratio of the capacitive and  
52  
53  
54  
55  
56  
57  
58  
59  
60  
61  
62  
63  
64  
65

1  
2  
3  
4 diffusion contribution was observed with  $\text{Na}_{0.7}\text{MnO}_{2.05}$ , while in the case of  $\text{Na}_{0.4}\text{MnO}_2$ , even at  
5  
6 lower scan rates, the capacitive contribution was over 90%.  
7  
8

9 Specific capacity was calculated from cyclic voltammograms recorded using a sweep rate  
10 of 20 mV/s as the area of the reduction peaks. The initial discharge capacity of  $\text{Na}_{0.4}\text{MnO}_2$  in  
11  $\text{NaNO}_3$  solution is 50 mAh/g, while after 15<sup>th</sup> cycle its values increased for 9%. During cycling,  
12 material has demonstrated great efficiency (the ratio of the charge/discharge capacity) amounting  
13 to ~ 95%. For  $\text{Na}_{0.7}\text{MnO}_{2.05}$  synthesized at 850 °C, the initial discharge capacity (after the first ten  
14 cycles during which the electrode was activated [15,42]) was 75 mAh/g. After an additional ten  
15 cycles, the capacity was increased to 79 mAh/g, or for 5%. During cycling,  $\text{Na}_{0.7}\text{MnO}_{2.05}$  has also  
16 shown very good efficiency of 97%. The initial discharge capacity for  $\text{Na}_{0.44}\text{MnO}_2$  synthesized at  
17 900 °C was 46 mAh/g, which after ten cycles was increased to 119 mAh/g, or for 158%.  
18  $\text{Na}_{0.44}\text{MnO}_2$  has also shown very good efficiency of 96%.  
19  
20  
21  
22  
23  
24  
25  
26  
27  
28  
29  
30  
31  
32

33 Since among investigated electrodes,  $\text{Na}_{0.44}\text{MnO}_2$  synthesized at 900 °C has shown the  
34 best cycling reversibility and specific capacity, its charge/discharge behavior will be examined in  
35 more details by chronopotentiometry.  
36  
37  
38  
39  
40  
41  
42

### 43 *3.3.2. Charge/discharge behavior for $\text{Na}_{0.44}\text{MnO}_2$ synthesized at 900 °C determined using* 44 *chronopotentiometry technique* 45 46 47

48 Chronopotentiometry measurements were performed for  $\text{Na}_{0.44}\text{MnO}_2$  electrode  
49 synthesized at 900 °C in a saturated aqueous  $\text{NaNO}_3$  solution, and the obtained results are  
50 presented in Fig. 7.  
51  
52  
53

54 Charge/discharge curves for the first cycle are presented in Fig. 7a. The specific capacities  
55 were calculated from these curves by multiplying the discharge times with each applied current  
56  
57  
58  
59  
60  
61  
62  
63  
64  
65

1  
2  
3  
4 density,  $t(s) \times j(\text{mA/g})$ , Fig. 7b. For the current densities of 1000, 2000, and 5000 mA/g, the  
5  
6 calculated discharge capacities were: 123.5, 113.2, and 102.0 mAh/g, respectively. After the 5th  
7  
8 cycle, the discharge capacities were slightly increased for all current rates, and the obtained  
9  
10 values for the current densities of 1000, 2000, and 5000 mA/g were 123, 113 and 102 mAh/g,  
11  
12 respectively. The discharge capacity is practically only slightly changed at very high current  
13  
14 densities, which indicates the superiority of the pseudo-capacitance in the total charge storage  
15  
16 behavior [26,44]. Furthermore, the same was confirmed based on the appearance of different  
17  
18 discharge/charge voltage profiles of  $\text{Na}_{0.44}\text{MnO}_2$  in aqueous and non-aqueous solution [27].  
19  
20  
21

22  
23  
24 Results show that for  $\text{Na}_{0.44}\text{MnO}_2$  electrode obtained at 900 °C, with increasing current  
25  
26 density, the charging and discharging processes slow down, while the capacity increases.  
27  
28 Therefore, this electrode is suitable for sodium-ion intercalation/deintercalation and eligible as a  
29  
30 cathode for Na-ion batteries.  
31  
32  
33  
34  
35

#### 36 **4. Conclusion**

37  
38  
39  
40

41  $\text{Na}_x\text{MnO}_2$  powders were synthesized by glycine nitrate method (GNM), and subsequent  
42  
43 annealing at three different temperatures: 800 °C, 850 °C, and 900 °C. Detailed structural,  
44  
45 morphological and chemical analysis has been performed, as well as the investigation of their  
46  
47 electrochemical performance for a potential use as cathodic materials for sodium-ion  
48  
49 rechargeable batteries.  
50  
51

52  
53 By X-ray diffraction analysis has confirmed the crystalline structure of obtained powders  
54  
55 identified as:  $\text{Na}_{0.7}\text{MnO}_{2.05}$  with a layered structure, which was obtained at 850 °C, and tunnel  
56  
57 structured  $\text{Na}_{0.4}\text{MnO}_2$  and  $\text{Na}_{0.44}\text{MnO}_2$  nanorods with different morphology, which were obtained  
58  
59 at 900 °C and 900 °C, respectively.  
60  
61  
62  
63  
64  
65

1  
2  
3  
4 SEM microscopy have shown that obtained powders have different morphology. Namely,  
5  
6 layer structured  $\text{Na}_{0.7}\text{MnO}_{2.05}$  consists of nanoplatets with the average diameter of several  
7  
8 micrometers, and the average width of several hundred nanometers. Tunnel structured  
9  
10  $\text{Na}_{0.4}\text{MnO}_2$  consists of nanorods 200 to 700 nm long and 60 to 110 nm wide, while  $\text{Na}_{0.44}\text{MnO}_2$   
11  
12 consists of much larger nanorods, approximately one micron long and few hundred nanometers  
13  
14 wide. Surface elemental mapping have shown the distribution of Na, Mn and O as the identified  
15  
16 elements. The chemical compositions of the samples and the oxidation state of Na, Mn and O in  
17  
18 each powder sample were identified by XPS technique.  
19  
20  
21  
22

23  
24 The electrochemical behavior of obtained powders has been investigated by cyclic  
25  
26 voltammetry and chronopotentiometry. Since  $\text{Na}_{0.44}\text{MnO}_2$  synthesized at 900 °C exhibits the best  
27  
28 properties concerning capacity and stability, it would be chosen as the best candidate for a  
29  
30 cathode in sodium-ion batteries.  
31  
32  
33  
34  
35

36 **Acknowledgement:** The work was supported by the Ministry of Education, Science and  
37  
38 Technological Development, Republic of Serbia.  
39  
40  
41  
42  
43  
44  
45  
46  
47  
48  
49  
50  
51  
52  
53  
54  
55  
56  
57  
58  
59  
60  
61  
62  
63  
64  
65

## References

- [1] Y. Liang, C-Z Zhao, H. Yuan, Y. Chen, W. Zhang, J-Q Huang, D. Yu, Y. Liu, M-M. Titirici, Y-L Chueh, H. Yu, Q. Zhang, A review of rechargeable batteries for portable electronic devices, *InfoMat*, 1 (2019) 6-32.
- [2] F. Wu, J. Maier, Y. Yu, Guidelines and trends for next-generation rechargeable lithium and lithium-ion batteries, *Chemical Society Reviews*, 49 (2020) 1569-1614.
- [3] J.Y. Hwang, S.T. Myung, Y.K. Sun, Sodium-ion batteries: present and future, *Chemical Society Reviews*, 46 (2017) 3529-3614.
- [4] X. Xiang, K. Zhang, J. Chen, Recent Advances and Prospects of Cathode Materials for Sodium-Ion Batteries, *Advanced Materials*, 27 (2015) 5343-5364.
- [5] W. Zhang, F. Zhang, F. Ming, H.N. Alshareef, Sodium-ion battery anodes: Status and future trends, *EnergyChem*, 1 (2019) 100012.
- [6] X. Pu, H. Wang, D. Zhao, H. Yang, X. Ai, S. Cao, Z. Chen, Y. Cao, Recent progress in rechargeable sodium-ion batteries: toward high-power applications, *Small*, 15 (2019) 1805427.
- [7] J. Liu, C. Xu, Z. Chen, S. Ni, Z.X. Shen, Progress in aqueous rechargeable batteries, *Green Energy & Environment*, 3 (2018) 20-41.
- [8] D. Bin, F. Wang, A. G. Tamirat, L. Suo, Y. Wang, C. Wang, Y. Xia, Progress in aqueous rechargeable sodium-ion batteries, *Advanced Energy Materials*, 8 (2018) 1703008.
- [9] R. Demir-Cakan, M. Rosa Palacin, L. Croguennec, Rechargeable aqueous electrolyte batteries: from univalent to multivalent cation chemistry, *Journal of Materials Chemistry A*, 7 (2019) 20519-20539.
- [10] M. Liu, H. Ao, Y. Jin, Z. Hou, X. Zhang, Y. Zhu, Y. Qian, Aqueous rechargeable sodium ion batteries: developments and prospects, *Materials Today Energy*, 17 (2020) 100432.



- 1  
2  
3  
4 [11] M. Xu, Y.Niu, Y. Li, S. Bao, C.M Li, Synthesis of sodium manganese oxides with  
5  
6 tailored multi-morphologies and their application in lithium/sodium-ion batteries, *RSC Advances*,  
7  
8 4 (2014) 30340-30345.  
9  
10  
11 [12] R.J. Clément, P.G. Bruce, C.P. Grey, Review - manganese-based P2-type transition metal  
12  
13 oxides as sodium-ion battery cathode materials, *Journal of The Electrochemical Society*, 162,  
14  
15 (2015) A2589-A2604.  
16  
17  
18 [13] K. Kubota, N. Yabuuchi, H. Yoshida, M. Dahbi, S. Komaba, Layered oxides as positive  
19  
20 electrode materials for Na-ion batteries, *Materials Research Bulletin*, 39 (2014) 416-422.  
21  
22  
23 [14] J.P. Parant, R. Olazcuaga, M. Devalette, C. Fouassier, P. Hagemuller, Sur quelques  
24  
25 nouvelles phases de formule  $\text{Na}_x\text{MnO}_2$  ( $x \leq 1$ ), *Journal of Solid State Chemistry*, 3 (1971) 1-11.  
26  
27  
28 [15] Y. Hou, H. Tang, B. Li, K. Chang, Z. Chang, X.-Z. Yuan, H. Wang, Hexagonal-layered  
29  
30  $\text{Na}_{0.7}\text{MnO}_{2.05}$  via solvothermal synthesis as an electrode material for aqueous Na-ion  
31  
32 supercapacitors, *Materials Chemistry and Physics*, 171 (2016) 137-144.  
33  
34  
35 [16] F.Sauvage, L. Laffont, J.-M. Tarascon, E. Baudrin, Study of the Insertion/Deinsertion  
36  
37 Mechanism of Sodium into  $\text{Na}_{0.44}\text{MnO}_2$ , *Inorganic Chemistry*, 46 (2007) 3289-3294.  
38  
39  
40 [17] E. Hosono, H. Matsuda, I. Honma, S. Fujihara, M. Ichihara, H. Zhou, Synthesis of single-  
41  
42 crystalline electro-conductive  $\text{Na}_{0.44}\text{MnO}_2$  nanowires with high aspect ratio for the fast charge-  
43  
44 discharge Li-ion battery, *Journal of Power Sources*, 182, (2008) 349-352.  
45  
46  
47 [18] Y. Cao, L. Xiao, W. Wang, D. Choi, Z. Nie, J. Yu, L.V. Saraf, Z. Yang, J. Liu, Reversible  
48  
49 sodium ion insertion in single-crystalline manganese oxide nanowires with long cycle life,  
50  
51 *Advanced Materials*, 23 (2011) 3155-3160.  
52  
53  
54 [19] L. Zhao, J. Ni, H. Wang, L. Gao, Flux synthesis of  $\text{Na}_{0.44}\text{MnO}_2$  nanoribbons and their  
55  
56 electrochemical properties for Na-ion batteries, *Functional Materials Letters*, 6 (2013) 1350012  
57  
58  
59  
60  
61  
62  
63  
64  
65

- 1  
2  
3  
4 [20] F. Hu, M. Doeff, Electrochemical characterization of manganese oxide cathode materials  
5 based on  $\text{Na}_{0.4}\text{MnO}_2$ , *Journal of Power Sources*, 129 (2004) 296-302.  
6  
7  
8  
9 [21] S. Liu, C-Z. Fan, Y. Zhang, C-H. Li, X-Z. You, Low-temperature synthesis of  $\text{Na}_2\text{Mn}_5\text{O}_{10}$   
10 for supercapacitor applications, *Journal of Power Sources*, 196 (2011) 10502-10506.  
11  
12  
13 [22] D. Su, C. Wang, H-J Ahn, G. Wang, Single Crystalline  $\text{Na}_{0.7}\text{MnO}_2$  nanoplates as cathode  
14 materials for sodium ion batteries with enhanced performance, *Chemistry A European Journal*  
15 19, (2013) 10884-10889.  
16  
17  
18  
19 [23] Y. Zhang, Z. Liu, H. Deng, J. Xie, J. Xia, S. Nie, W. Liu, L. Liu, X. Wang, Rectangular  
20 tunnel-structured  $\text{Na}_{0.4}\text{MnO}_2$  as a promising cathode material withstanding a high cutoff voltage  
21 for Na-ion batteries, *ChemElectroChem* 2019, 6, 1–12.  
22  
23  
24  
25 [24] D.J. Kim, R. Ponraj, A.G. Kannan, H.W. Lee, R. Fathi, R. Ruffo, C.M. Mari, D.K. Kim,  
26 Diffusion behavior of sodium ions in  $\text{Na}_{0.44}\text{MnO}_2$  in aqueous and non-aqueous electrolytes.  
27 *Journal of Power Sources*, 244 (2013) 758-763.  
28  
29  
30  
31 [25]. M.S. Chae, A. Chakraborty, S. Kunnikuruvan, R. Attias, S. Maddakuri, Y. Gofer, D.T.  
32 Major, D. Aurbach, Vacancy-driven high rate capabilities in calcium-doped  $\text{Na}_{0.4}\text{MnO}_2$  Cathodes  
33 for Aqueous Sodium-Ion Batteries, *Advanced Energy Materials*, (2020) 2002077.  
34  
35  
36 [26] J. Li, L. Li, H. Shi, Z. Zhong, X. Niu, P. Zeng, Z. Long, X. Chen, J. Peng, Z. Luo, X. Wang,  
37 S. Liang, Electrochemical energy storage behavior of  $\text{Na}_{0.44}\text{MnO}_2$  in aqueous zinc-ion battery,  
38 *ACS Sustainable Chemistry & Energy*, 8 (2020) 10673-10681.  
39  
40  
41  
42 [27] Y. Wang, J. Liu, B. Lee, R. Qiao, Z. Yang, S. Xu, X. Yu, L. Gu, Y-S. Hu, W. Yang, K.  
43 Kang, H. Li, X-Q. Yang, L. Chen, X. Huang, Ti-substituted tunnel-type  $\text{Na}_{0.44}\text{MnO}_2$  oxide as a  
44 negative electrode for aqueous sodium-ion batteries, *Nature Communications*, 6 (2015) 1-10.  
45  
46  
47  
48  
49  
50  
51  
52  
53  
54  
55  
56  
57  
58  
59  
60  
61  
62  
63  
64  
65

- 1  
2  
3  
4 [28] H. Li, S. Liu, T. Yuan, B. Wang, P. Sheng, L. Xu, G. Zhao, H. Bai, X. Chen, Z. Chen, Y.  
5  
6 Cao, Electrochemical mechanism of  $\text{Na}_{0.44}\text{MnO}_2$  in alkaline aqueous solution, *Acta Physico-*  
7  
8 *Chimica Sinica* 36 (2020), 1905027.
- 9  
10  
11 [29] National Bureau of Standards, *Standard X-ray diffraction powder patterns*, 539 (1959) 37.
- 12  
13  
14 [30] J. Du, G. Xiao, Y. Xi, X. Zhu, F. Su, S.H. Kim, Periodate activation with manganese oxides  
15  
16 for sulfanilamide degradation. *Water Research*, 169 (2020) 115278.
- 17  
18  
19 [31] Z.Y. Leong, H.Y. Yang, A study of  $\text{MnO}_2$  with different crystalline forms for  
20  
21 pseudocapacitive desalination, *ACS Applied Materials & Interfaces*, 11 (2019) 13176-13184.
- 22  
23  
24 [32] S. Patoux, M. Dollé, M.M. Doeff, Layered manganese oxide intergrowth electrodes for  
25  
26 rechargeable lithium batteries. 2. Substitution with Al, *Chemistry of Materials*, 20 (2005) 1044–  
27  
28 1054.
- 29  
30  
31 [33] X. He, J. Wang, B. Qiu, E. Paillard, C. Ma, X. Cao, H. Liu, M. C. Stan, H. Liu, T. Gallash,  
32  
33 Y.S. Meng, J. Li, Durable high-rate capability  $\text{Na}_{0.44}\text{MnO}_2$  cathode material for sodium-ion  
34  
35 batteries, *Nano Energy*, 27 (2016) 602–610.
- 36  
37  
38 [34] A. Barrie, F.J. Street, An Auger and X-ray photoelectron spectroscopic study of sodium  
39  
40 metal and sodium oxide, *Journal of Electron Spectroscopy and Related Phenomena*, 7 (1975) 1-  
41  
42 31.
- 43  
44  
45 [35] P.H. Citrin, High-resolution X-ray photoemission from sodium metal and its hydroxide,  
46  
47 *Physical Review B*, 8 (1973) 5545-5556.
- 48  
49  
50 [36] M.C. Biesinger, B.P. Payne, A.P. Grosvenor, L.W.M. Lau, A.R. Gerson, R.St.C. Smart,  
51  
52 Resolving surface chemical states in XPS analysis of first-row transition metals, oxides, and  
53  
54 hydroxides: Cr, Mn, Fe, Co and Ni, *Applied Surface Science* 257 (2011) 2717–2730.
- 55  
56  
57  
58  
59  
60  
61  
62  
63  
64  
65

- 1  
2  
3  
4 [37] H.W. Nesbitt, D. Banerjee, Interpretation of XPS Mn(2p) spectra of Mn oxy-hydroxides and  
5 constraints on the mechanism of MnO<sub>2</sub> precipitation, *American Mineralogist*, **83** (1998) 305.  
6  
7  
8  
9 [38] M. Oku, K. Hirokawa, X-ray photoelectron spectroscopy of manganese-oxygen systems,  
10 *Journal of Electron Spectroscopy and Related Phenomena*, 7 (1975) 465-473.  
11  
12  
13  
14 [39] H. Lin, D. Chen, H. Liu, X. Zou, T. Chen, Effect of MnO<sub>2</sub> Crystalline structure on the  
15 catalytic oxidation of formaldehyde, *Aerosol and Air Quality Research*, 17 (2017) 1011–1020.  
16  
17  
18  
19 [40] M. Oku, X-ray photoelectron spectra of KMnO<sub>4</sub> and K<sub>2</sub>MnO<sub>4</sub> fractured in situ, *Journal of*  
20 *Electron Spectroscopy and Related Phenomena*, 74 (1995) 135-148.  
21  
22  
23  
24 [41] Z. Shuxian , W.K. Hall, G. Ertl, H. Knozinger, X-ray photoemission study of oxygen and  
25 nitric oxide adsorption on MoS<sub>2</sub>, *Journal of Catalysis*, 100 (1986) 167-175.  
26  
27  
28  
29 [42] T.R. Chen, Z-G. Wu, W. Xiang, E-H. Wang, C-J. Wu, M-Z. Chen, X-D. Guo, B-H. Zhong,  
30 The influences of sodium sources on the structure evolution and electrochemical performances of  
31 layered-tunnel hybrid Na<sub>0.6</sub>MnO<sub>2</sub> cathode, *Ceramics International*, 43 (2017) 6303-6311.  
32  
33  
34  
35 [43] F. Sauvage, E. Baudrin, J-M. Tarascon, Study of the potentiometric response towards  
36 sodium ions of Na<sub>0.44-x</sub>MnO<sub>2</sub> for the development of selective sodium ion sensors, *Sensors and*  
37 *Actuators B*, 120 (2007) 638–644.  
38  
39  
40  
41 [44] C. Choi, D.S. Ashby, D.M. Butts, R.H. DeBlock, Q. Wei, J. Lau, B. Dunn, Achieving high  
42 energy density and high power density with pseudocapacitive materials. *Nature Review*  
43 *Materials*, 5 (2020) 5–19.  
44  
45  
46  
47  
48  
49  
50  
51  
52  
53  
54  
55  
56  
57  
58  
59  
60  
61  
62  
63  
64  
65

1  
2  
3  
4  
5  
6  
7  
8  
9  
10  
11  
12  
13  
14  
15  
16  
17  
18  
19  
20  
21  
22  
23  
24  
25  
26  
27  
28  
29  
30  
31  
32  
33  
34  
35  
36  
37  
38  
39  
40  
41  
42  
43  
44  
45  
46  
47  
48  
49  
50  
51  
52  
53  
54  
55  
56  
57  
58  
59  
60  
61  
62  
63  
64  
65

1  
2  
3  
4  
5  
6  
7 **Figure Captions**  
8

9 **Fig. 1.** XRD diffractograms (left column) and corresponding SEM micrographs magnified 20000  
10 times (right column) of  $\text{Na}_x\text{MnO}_2$  powders synthesized at: a,b) 800 °C; c,d) 850 °C; e,f) 900 °C.  
11  
12

13 **Fig. 2.**EDS elemental mapping images of  $\text{Na}_x\text{MnO}_2$  powders synthesized at 800 °C, 850 °C, and  
14 900 °C.  
15  
16

17 **Fig. 3.** Survey XPS spectrum of  $\text{Na}_x\text{MnO}_2$  powder.  
18  
19

20 **Fig. 4.** High resolution spectra of  $\text{Mn}2p_{3/2}$ ,  $\text{Na}1s$  and  $\text{O}1s$  lines for  $\text{Na}_x\text{MnO}_2$  powders  
21 synthesized at: a) 800 °C; b) 850 °C; c) 900 °C.  
22  
23

24 **Fig. 5.** CVs of  $\text{Na}_x\text{MnO}_2$  electrodes synthesized at different temperatures: a) 800 °C; b) 850 °C;  
25 c) 900 °C. CVs were recorded in saturated aqueous  $\text{NaNO}_3$  during continuous cycling with a  
26 sweep rate of 20 mV/s.  
27  
28

29 **Fig. 6.** Comparison of electrochemical performance of  $\text{Na}_x\text{MnO}_2$  synthesized at different  
30 temperatures: (a, d, g) cyclic voltammograms recorded in saturated aqueous  $\text{NaNO}_3$  with  
31 different sweep rates within the range of 20-400 mV/s, (b, e, h)  $\log(i)$  vs  $\log(v)$  plots at specific  
32 peak currents, and (c, f, i) the average contribution ratio of diffusion and capacitive controlled  
33 process.  
34  
35

36 **Fig. 7.**Chronopotentiometry results for  $\text{Na}_{0.44}\text{MnO}_2$  electrodes synthesized at 900 °C obtained for  
37 the current rates of 1000, 2000, and 5000  $\text{mA g}^{-1}$  in saturated aqueous  $\text{NaNO}_3$ : a)  
38 charge/discharge curves; b) discharge capacity vs. number of cycles.  
39  
40  
41  
42  
43  
44  
45  
46  
47  
48  
49  
50  
51  
52  
53  
54  
55  
56  
57  
58  
59  
60  
61  
62  
63  
64  
65

Figure 1

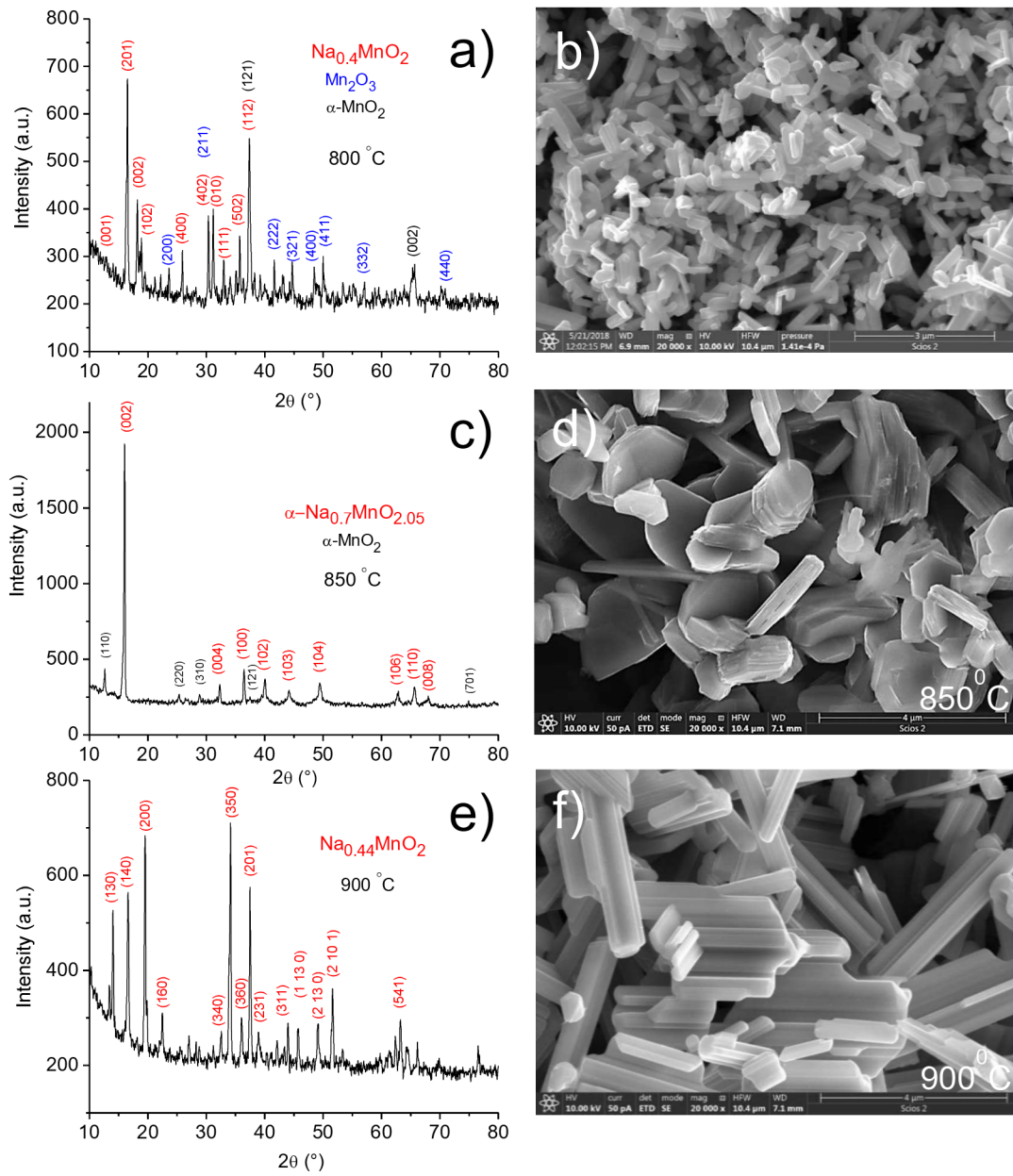


Fig. 1

Figure 2

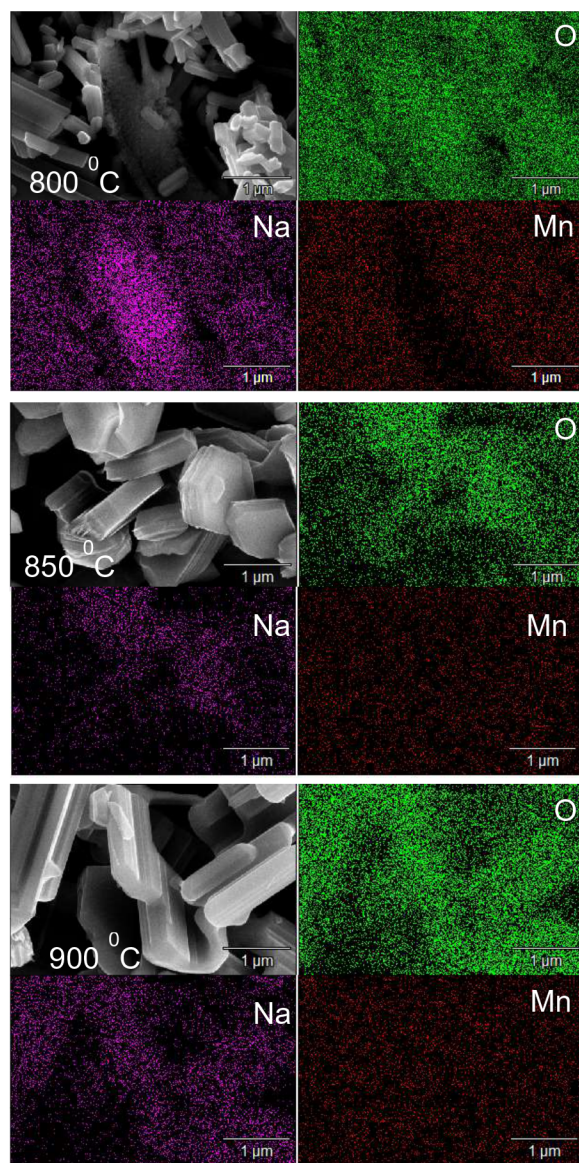


Fig. 2



Figure 3

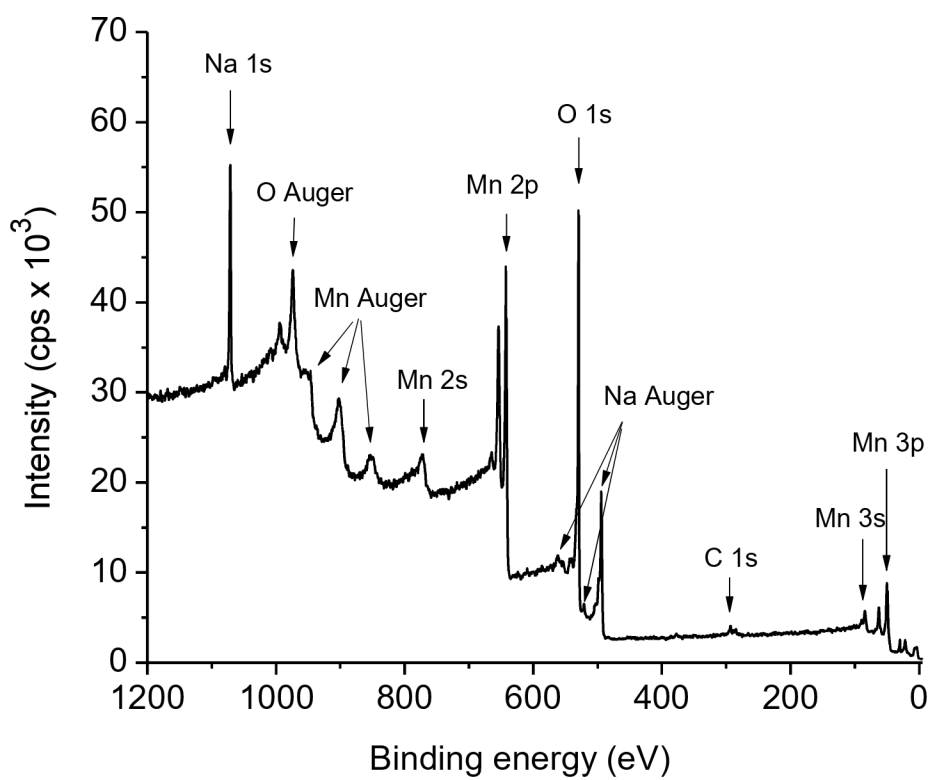


Fig. 3

Figure 4

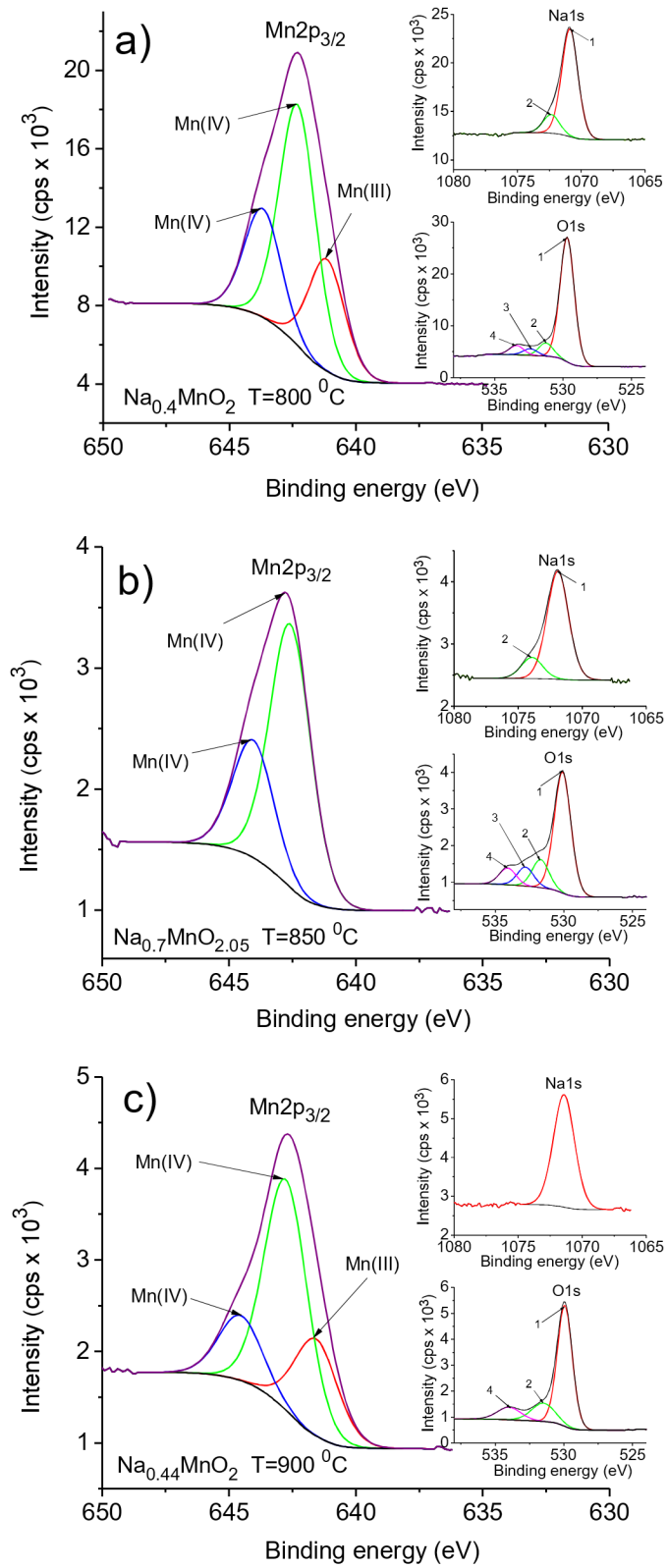


Fig. 4

Figure 5

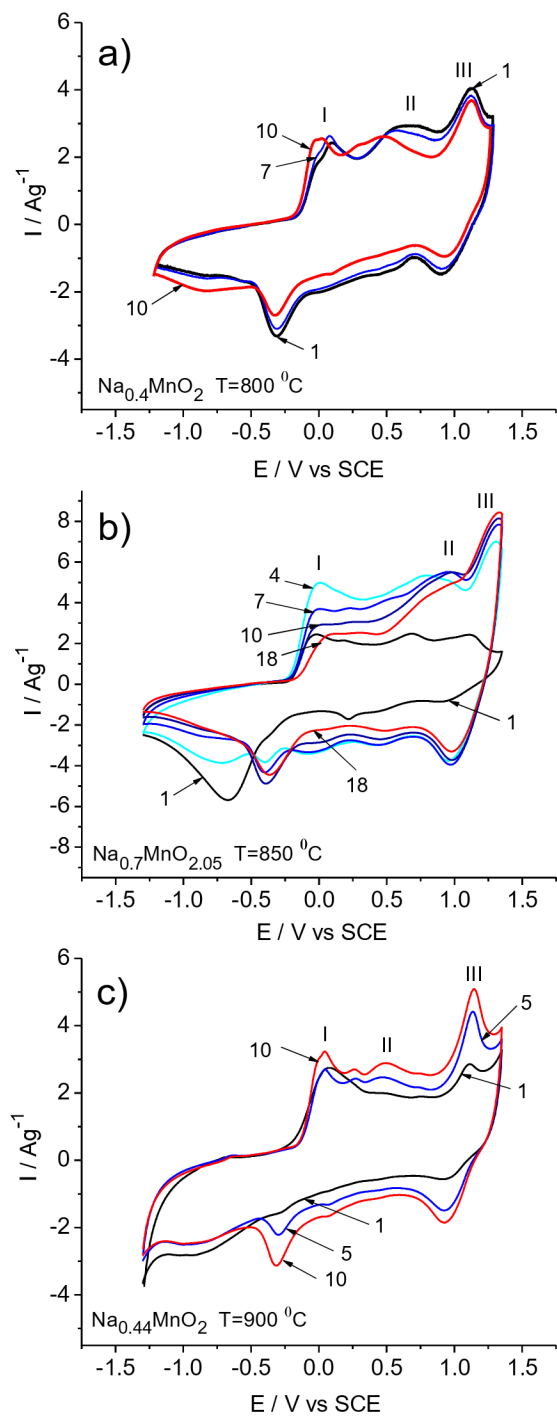


Fig. 5

Figure 6

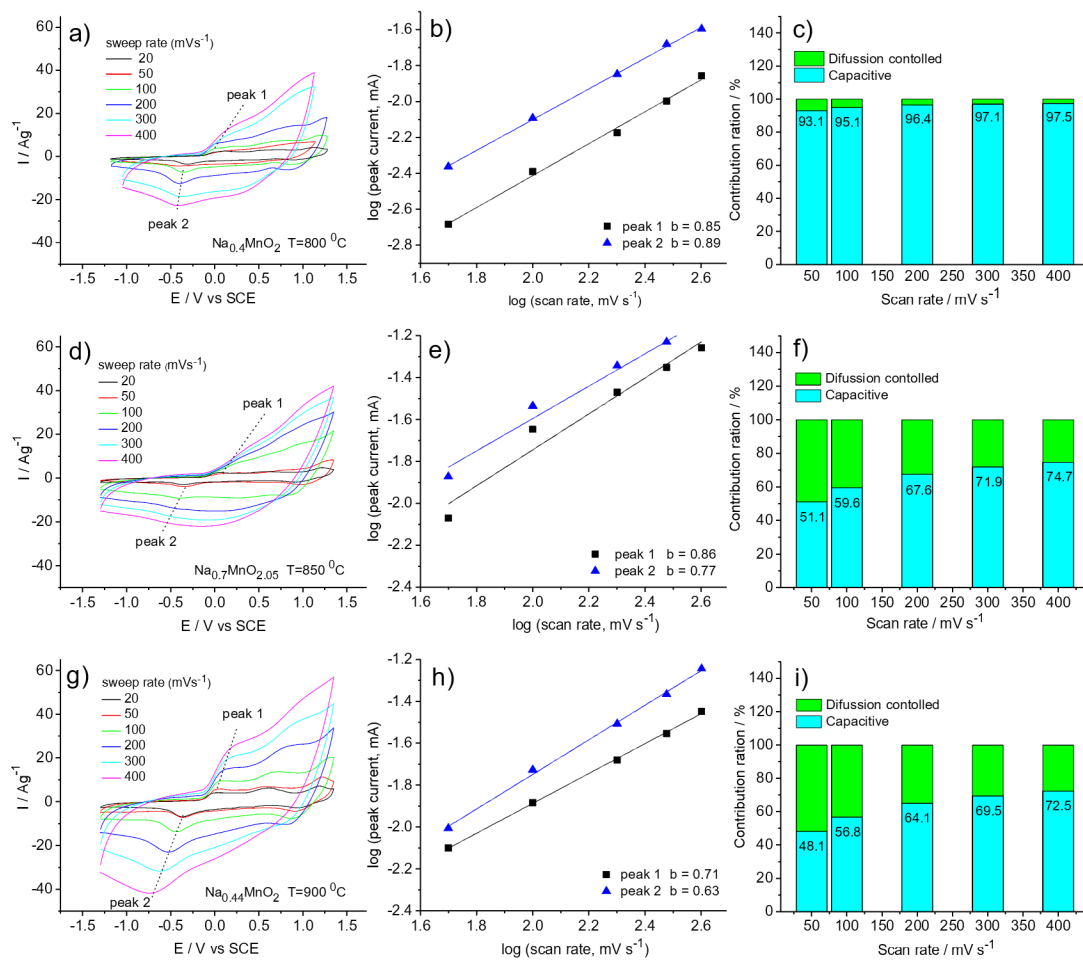


Fig. 6

Figure 7

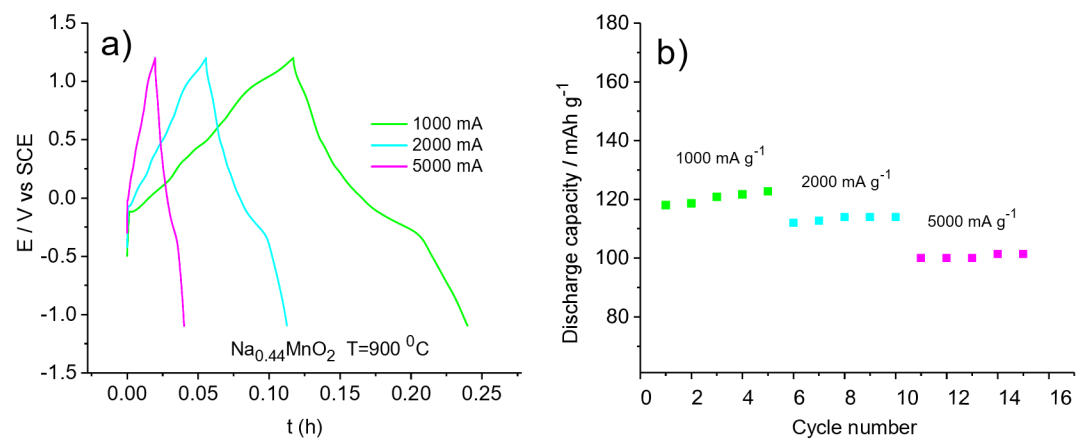


Fig. 7